Universal scattering response in the type-II Weyl semimetals phase diagram - Supplemental Material

P. Rüßmann,[1] A. P. Weber,[2,3] F. Glott,[4] N. Xu,[2,3] M. Fanciulli,[2,3] S. Muff,[2,3] A. Magrez,[2] P. Bugnon,[2] H. Berger,[2] M. Bode,[4] J. H. Dil,[2,3] S. Blügel,[1] P. Mavropoulos,[1] and P. Sessi[4,*]

[1]*Peter Grünberg Institut and Institute for Advanced Simulation, Forschungszentrum Jülich and JARA, 52425 Jülich, Germany*

[2]*Institute of Physics, École Polytechnique Fédérale de Lausanne, 1015 Lausanne, Switzerland*

[3]*Swiss Light Source, Paul Scherrer Institute, 5232 Villigen-PSI, Switzerland*

[4]*Physikalisches Institut, Experimentelle Physik II, Universität Würzburg, Am Hubland, D-97074 Würzburg, Germany*

(Dated: January 12, 2018)

* corresponding author: sessi@physik.uni-wuerzburg.de

CONTENTS

I. DFT CALCULATIONS

A. Computational details

1. Bulk and thin film calculations

In our density functional theory calculations we employ the full-potential relativistic Korringa-Kohn-Rostoker Green function method (KKR). We use the experimental low-temperature structure for $MoTe_2$ and WTe_2 [55,56], the local spin density approximation (LSDA) for the exchange-correlation functional [57] and we correct for the truncation error due to the finite angular momentum cutoff of $l_{\max} = 3$ by using Lloyd's formula [34]. The full potential treatment includes corrections for the exact shape of the atomic cells [58,59]. The convergence of the calculation was checked with respect to the k-point grid and energy contour integration.

The calculated band structures along high symmetry lines and the Fermi surfaces are in good agreement with previously published data on $MoTe_2$ and WTe_2 [60,61]. However, in contrast to the calculations in Ref. [61] we do not find Weyl points for WTe_2 but we obtain an energy gap of $\sim$ 15meV instead. It is known that the exact location of the transition to the Weyl-II phase can be tuned with the lattice constant, spin-orbit strength, or doping between $MoTe_2$ and WTe_2 [62,63] so that the approximations entering the calculation may affect the outcome. In most of the literature, the calculations are based on Wannier functions with tight-binding parameters obtained within the pseudopotential package VASP. On the other hand, we use the all-electron KKR method and compute the band structure in the full Brillouin zone without the detour via Wannier-functions. Calculations by Aguilera with the all-electron full-potential augmented plane waves (FLAPW) method as implemented in the FLEUR code [64], using the generalized gradient approximation GGA exchange correlation functional [65], confirm the absence of Weyl points for WTe_2 [66]. Thus, we can conclude that the choice of exchange-correlation functional (LSDA *vs.* GGA) only plays a minor role in this case.

Thin film calculations were performed for a thickness of 8 triple layers (TL) which was chosen to ensure that the top and bottom surfaces decouple. We checked this by comparing the band structure with increasing thicknesses from 1TL ($\sim$ 4Å thin film) up to 8TL ($\sim$ 53Å thick film).

Based on the converged potentials the Fermi surface was computed with a very high accuracy [31,32]. Here a dense k-mesh with $\sim 10^6$ points in the surface Brillouin zone is necessary for the accurate calculation of exJDOS images (described below).

2. Impurity calculations

The embedding of single substitutional impurities was calculated self-consistently using the Dyson equation to obtain the impurity Green function [67]. Clusters including the atoms up to the third nearest neighbors were taken into account for a correct screening of the charge density around the impurity.

We considered a number of substitutional intrinsic defects in the outermost TL of $MoTe_2$ and WTe_2 films. The surface buckling in the T_d structure gives rise to two distinct positions in each layer (Te1/2 and TM1/2 on top and bottom surfaces, where TM stands for the transition metal atom Mo or W). The defects we considered were vacancies in the outermost Te layer ($Vc_{Te1/2}$), substitution of a Te atom by an intrinsic transition metal atom ($W_{Te1/2}$ in WTe_2 and $Mo_{Te1/2}$ in $MoTe_2$), and a Te atom in the outermost TM layer ($Te_{TM1/2}$). Both the top and bottom surfaces were considered as hosts, since they are inequivalent. They are indicated by a subscript "t" or "b", respectively. The orientation of the film, as it was used in the calculation, is given in Tab. I.

The calculated local density of states (LDOS) reveals that only the $TM_{Te1/2t}$ and TM_{Te1b} impurities show a resonance in the energy range of interest. The energy varies with respect to the different positions by less than 0.3eV (cf. Tab. II). These values are only approximative, since structural relaxations were ignored. A detailed analysis of LDOS spectra and simulated quasiparicle inteference (QPI) spectra using the exJDOS approach described below drove us to the conclusion that on $MoTe_2$ either the non-magnetic Mo_{Te1t} or the Mo_{Te2t} magnetic defect in the "top" surface was probed whereas on WTe_2 the W_{Te1b} defect in the "bottom" surface was probed.

3. Calculation of impurity scattering

Using the converged impurity potentials, the scattering properties of the different impurities were computed based on the calculation of the t-matrix $T_{\boldsymbol{k}'\boldsymbol{k}}$ and Fermi's Golden

TABLE I. Atomic positions, in units of the in-plane lattice constant a, in the first and second trilayer in $MoTe_2$ (left) (orthorombic structure with $a = 3.477\,\text{Å}$, $b = 6.335\,\text{Å}$, $c = 13.883\,\text{Å}$) [55] and for WTe_2 (right) (orthorombic structure with $a = 3.477\,\text{Å}$, $b = 6.429\,\text{Å}$, $c = 14.018\,\text{Å}$) [56]). Between subsequent $TMTe_2$ layers lies a layer with empty cells (EC) that is needed to account for the larger separation in the van der Walls gap. The "top" surface layer is the first line. In total, the unit cell consists of 12 atomic layers plus 4 empty cells (including empty cells), contained in two triple layer, where the buckling leads to the need of two positions per Te and TM layer.

element	x	y	z	element	x	y	z
Te	0.5	0.473	3.598	Te	0.5	0.465	3.626
Te	0.0	1.374	3.425	Te	0.0	1.353	3.449
Mo	0.0	0.664	3.035	W	0.0	0.646	3.061
Mo	0.5	0.000	2.977	W	0.5	0.000	3.000
Te	0.5	1.112	2.587	Te	0.5	1.085	2.613
Te	0.0	0.196	2.414	Te	0.0	0.184	2.435
EC	0.5	0.702	2.023	EC	0.5	0.680	2.033
EC	0.5	1.613	1.996	EC	0.5	1.579	2.016
Te	0.0	1.239	1.601	Te	0.0	1.189	1.611
Te	0.5	0.339	1.428	Te	0.5	0.301	1.433
Mo	0.5	1.048	1.038	W	0.5	1.008	1.046
Mo	0.0	1.712	0.981	W	0.0	1.654	0.984
Te	0.0	0.600	0.591	Te	0.0	0.569	0.598
Te	0.5	1.517	0.418	Te	0.5	1.470	0.420
EC	0.0	1.010	0.026	EC	0.0	0.974	0.018
EC	0.0	0.099	0.000	EC	0.0	0.075	0.000

rule for the transition rate, $P_{\boldsymbol{k}'\boldsymbol{k}} = \frac{2\pi}{\hbar}|T_{\boldsymbol{k}'\boldsymbol{k}}|^2\delta(E_{\boldsymbol{k}} - E_{\boldsymbol{k}'})$, between initial ($\boldsymbol{k}$) and final ($\boldsymbol{k}'$) states [33]. Here we focus on the scattering rates (inverse of the lifetime) of the states at different energies as well as the simulation of quasiparticle interference maps using the extended joint density of states (exJDOS) approach. The total scattering rate of a state $\boldsymbol{k}$ at energy E is defined as $\tau_{\boldsymbol{k}}^{-1} = \int \mathrm{d}k' v_{\boldsymbol{k}'}^{-1} P_{\boldsymbol{k}',\boldsymbol{k}}$ where the integration is performed over a

TABLE II. Calculated total energies of different TM_{Te2} substitutional defects with respect to the TM_{Te1} non-magnetic defect at top ("t") (first three columns) and bottom ("b") (last three colums) surfaces. "mag" stands for magnetic defect. Values are given in eV.

system\impurity	$TM_{Te1t,mag}$	TM_{Te2t}	$TM_{Te2t,mag}$	$TM_{Te1b,mag}$	TM_{Te2b}	$TM_{Te2b,mag}$
WTe_2	–	-0.10	-0.27	–	-0.06	-0.24
$MoTe_2$	-0.05	0.21	-0.20	-0.05	0.11	-0.27

constant-energy contour $E_{\boldsymbol{k}} = E_{\boldsymbol{k}'} = E$. The exJDOS [68] is also defined as an integral over the constant-energy contour at energy $E_{\boldsymbol{k}} = E_{\boldsymbol{k}+\boldsymbol{q}} = E$,

$$\mathrm{exJDOS}(\boldsymbol{q}; E) = \int \mathrm{d}k A^{\mathrm{surf}}_{\boldsymbol{k}}(E) M_{\boldsymbol{k},\boldsymbol{k}+\boldsymbol{q}}(E) A^{\mathrm{surf}}_{\boldsymbol{k}+\boldsymbol{q}}(E). \tag{1}$$

Here, $A^{\mathrm{surf}}_{\boldsymbol{k}}(E)$ is the spectral density integrated in the spatial region between STM tip and sample surface, and $M_{\boldsymbol{k}\boldsymbol{k}'}(E) = P_{\boldsymbol{k}\boldsymbol{k}'}(E)\, \gamma^{\mathrm{STM}}_{\boldsymbol{k}\boldsymbol{k}'}(E)$ where

$$\gamma^{\mathrm{STM}}_{\boldsymbol{k}\boldsymbol{k}'}(E) = 1 - \cos(\boldsymbol{v}_{\boldsymbol{k}}, \boldsymbol{v}_{\boldsymbol{k}'}) \tag{2}$$

accounts for the fact that STM probes standing waves, i.e., states with opposite group velocities are favored. The exJDOS is finally used to compare with experimentally observed quasiparticle interference (QPI) measurements.

4. STM-sensitivity factor in exJDOS calculations

The influence of the STM-sensitivity factor γ^{STM} defined above in Eq. (2) is demonstrated for $MoTe_2$ at $E - E_F = 60\,\mathrm{meV}$ in Fig. 1. The comparison of the panels without γ^{STM} [shown in (a)] and with the panel including the sensitivity factor [shown in (b)] reveals that the flat curvature of the Fermi arc leads to a more pronounced relative intensity for the QPI feature associated to inter-arc scattering (white dashed ellipses) if the backscattering sensitivity of the STM and thus the good nesting of the Fermi arc is accounted for.

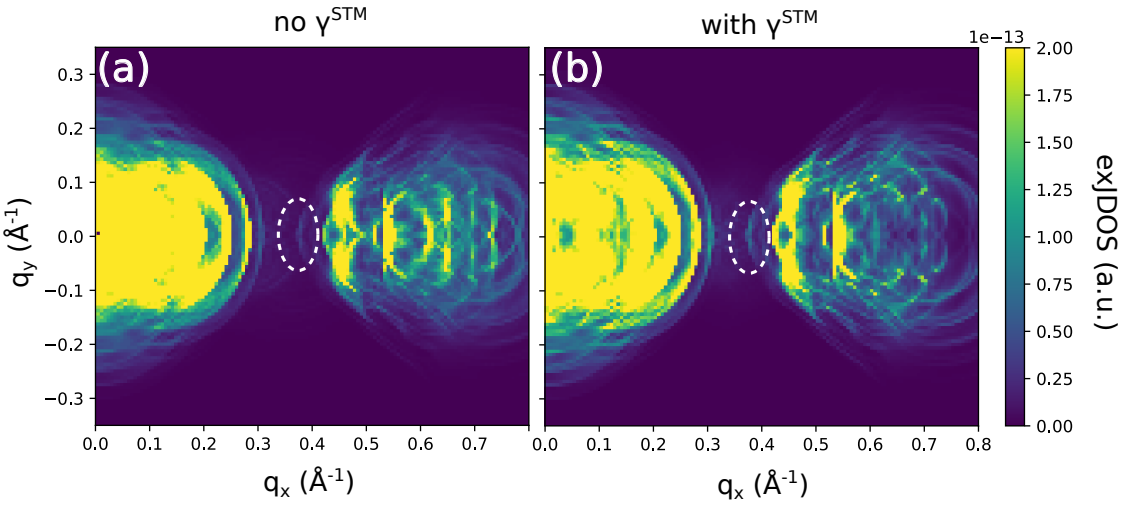

FIG. 1. exJDOS images (a) without and (b) with the STM-sensitivity factor γ^{STM} included in the calculation. Data of the exJDOS images were taken for the magnetic $\mathrm{Mo}_{\mathrm{Te2,mag}}$ impurity at $E = E_F + 60\,\mathrm{meV}$, which is discussed below in more detail. The contribution of the topological Fermi arc is highlighted with the white dashed ellipses where a higher intensity is seen in (b) as compared to (a) due to the good nesting in the relatively flat Fermi arc contour. The color scale was rescaled by a factor 5 as compared to Fig. 9 to highlight the changes in the strongly suppressed inter-arc contribution.

B. Thin-film electronic structure of WTe_2 and $MoTe_2$

1. *Surface state localization in $MoTe_2$ and WTe_2*

The T_d structure of $MoTe_2$ and WTe_2 is an orthorhombic crystal structure without inversion symmetry. Therefore, top and bottom surfaces are not equivalent which results in slightly different shape of the surface states at the two surfaces. This can be seen in Fig. 2 where the Fermi surfaces of WTe_2 and $MoTe_2$ are shown with the localization of the states indicated by blue (localized on top surface) and red (bottom surface) colors. The measure of localization is defined by $X = \frac{A-B}{A+B}$, where A and B are the integrated densities within the first and last trilayers in the film, respectively. The comparison of impurity spectra as well as ARPES data drove us to the conclusion that in $MoTe_2$ the "top" surface (blue states in Fig. 2) whereas in WTe_2 the "bottom" surface (red states) was probed.

In Figs. 3 and 4 we show the band structure of the thin film systems used in the calculations at cuts $k_y = 0.00$Å, 0.018Å, 0.036Å, 0.054Å, 0.072Å, and 0.090Å. The color

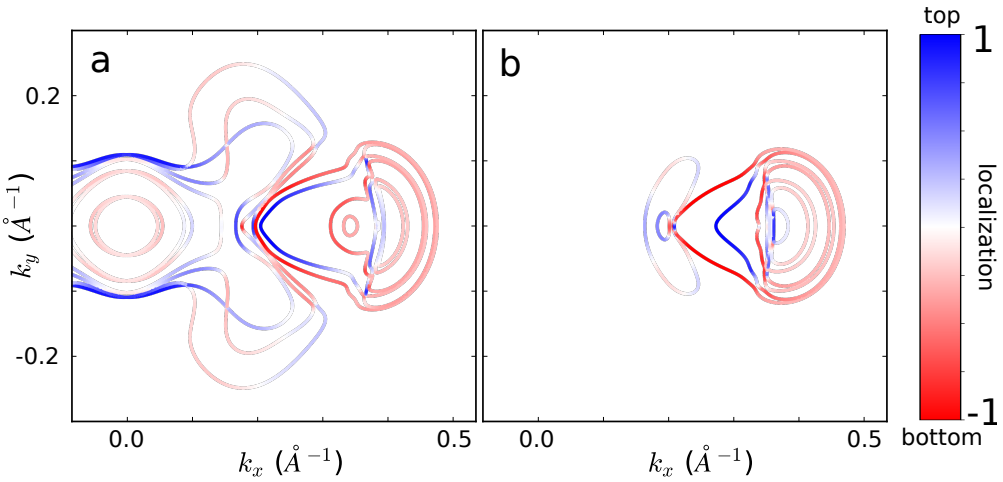

FIG. 2. Localization of the states in $MoTe_2$ (a) and WTe_2 (b). The color codes indicates the localization on top (blue) and bottom (red) surfaces that are inequivalent due to the lack of inversion symmetry.

code gives the surface/bulk character of the bands, where red colors denote a surface state and blue colors a bulk state. We defined a localization function

$$g_{\boldsymbol{k}}(E) = \frac{n^{1st}_{\boldsymbol{k}}(E) - n^{mid}_{\boldsymbol{k}}(E)}{n^{1st}_{\boldsymbol{k}}(E) + n^{mid}_{\boldsymbol{k}}(E)} \tag{3}$$

as measure of the localization of the state, where $n^{1st}_{\boldsymbol{k}}(E)$ is the $\boldsymbol{k}$ and energy-resolved density integrated in the layers of the first TL and $n^{mid}_{\boldsymbol{k}}(E)$ the integrated density of the 4th (i.e. middle) TL. Artifacts coming from states localized exponentially on the opposite surface, which would show up as blue colors due to the small contribution in the middle in combination with the even smaller contribution on the surface, were additionally suppressed to focus on the relevant surface ("top" surface of $MoTe_2$, "bottom" surface of WTe_2).

Although no touching points of the (blue) bulk bands are found between the valence band and conduction band in the topologically trivial WTe_2 (Fig. 3), a surface state (red) connects electron and hole pockets close to $k_y = 0$ (top row in Fig. 3). A similar band structure is found for the topologically nontrivial $MoTe_2$ system (Fig. 4), where, in addition to the red-colored surface state connecting electron and hole pockets, the touching of the bulk bands is visible between the fourth and fifth panel ($k_y = 0.054$Å and $k_y = 0.072$Å).

The bandstructures shown in Figs. 4 and 3 are illustrated in Fig. 1a of the main text, where the band structure evolution between the two extremes of the $Mo_xW_{1-x}Te_2$ phase diagram is depicted schematically.

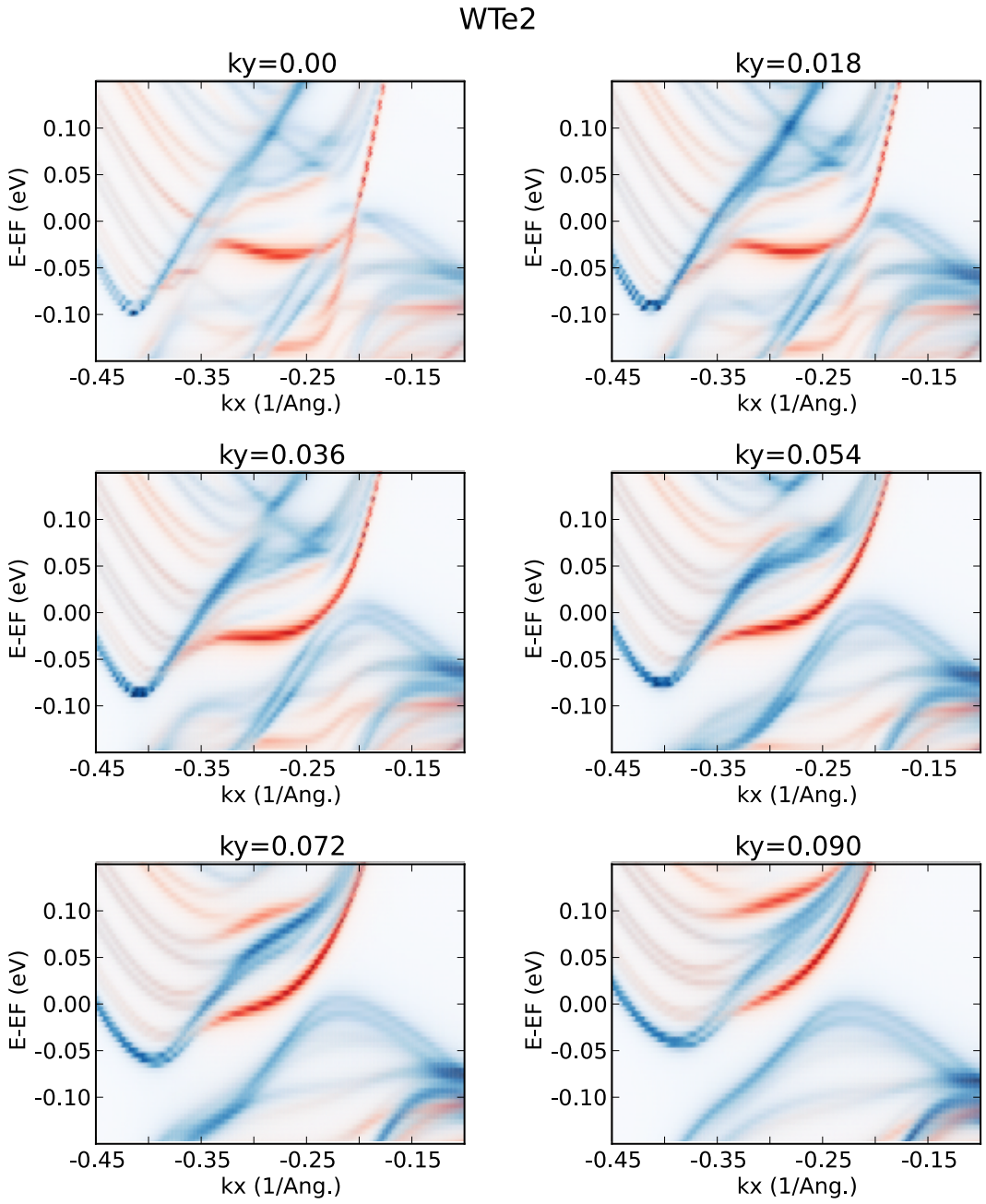

FIG. 3. Band structure cuts of WTe_2 along k_x for varying k_y between 0 and 0.09Å^{-1} from the top left to bottom right panels. The color code indicates the band character, which is defined in the text and where red and blue colors denote, respectively, surface and bulk character of the bands. For the surface only the contribution from the "bottom" surface of the WTe_2 is shown (red colors), which is the surface used in the remainder of the calculations.

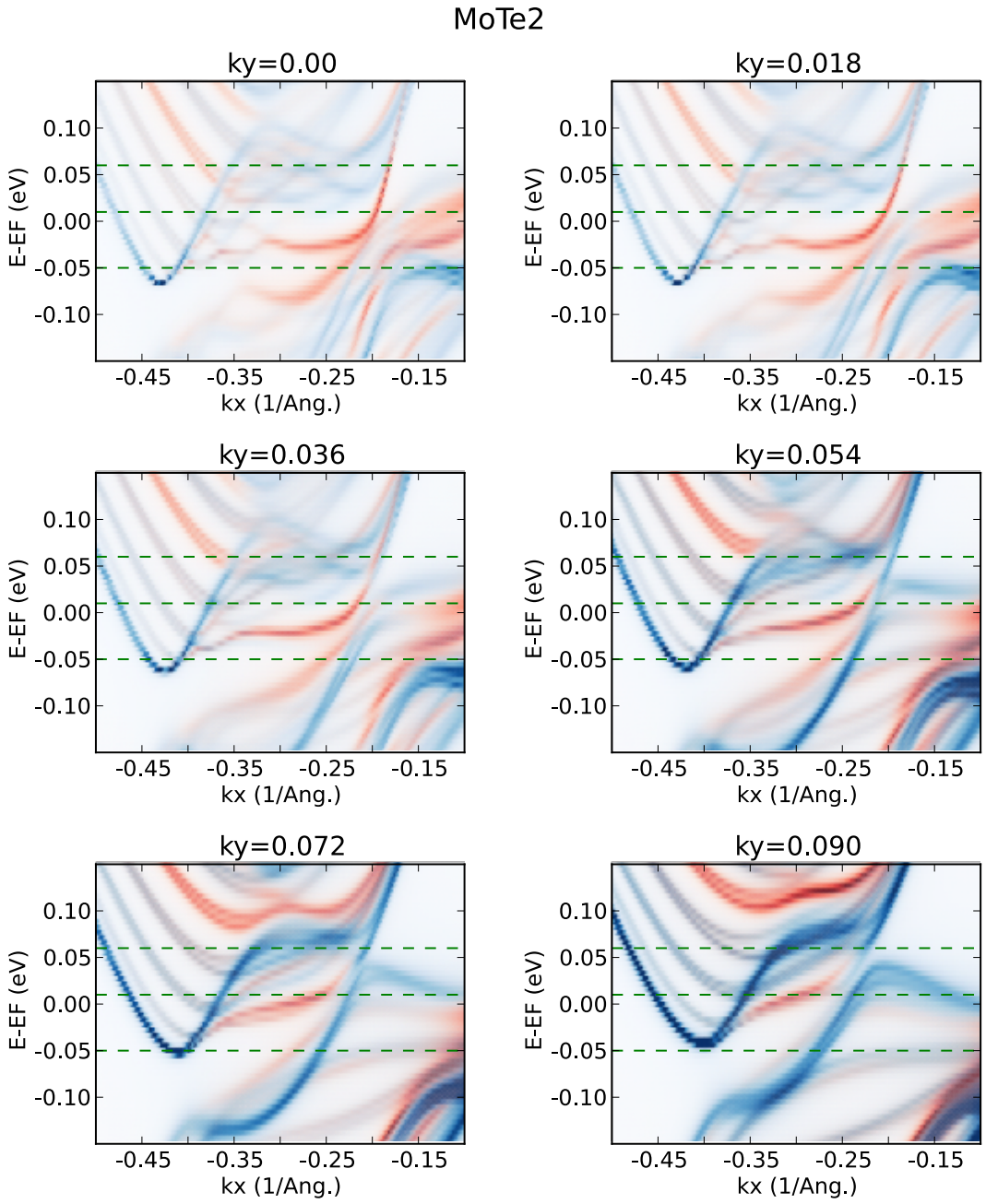

FIG. 4. Band structure cuts of $MoTe_2$ along k_x for varying k_y between 0 and 0.09Å^{-1} from the top left to bottom right panels. The color code indicates the band character, which is defined in the text and where red and blue colors denote, respectively, surface and bulk character of the bands. For the surface only the contribution from the "top" surface of the $MoTe_2$ is shown (red colors), which is the surface used in the remainder of the calculations. The horizontal dashed green lines indicate the energies that are analyzed in detail in the main text in comparison of exJDOS simulations and measured FT-QPI images (cf. Fig. 4 of the main text).

2. Spin polarization in $MoTe_2$ at $E = E_F + 60\,\mathrm{meV}$

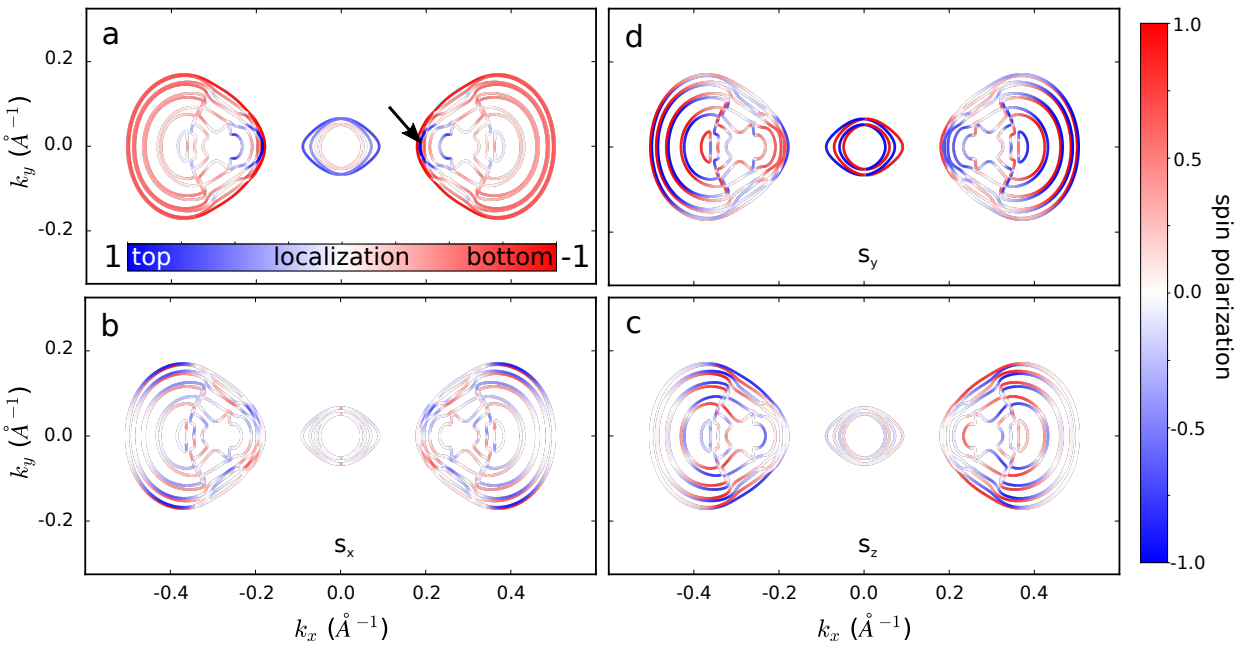

FIG. 5. Localization (a) and spin polarization for the surface states in $MoTe_2$. Given are x, y and z components of the spin polarization in (b–c). The topological Fermi arc, localized at the "top" surface, is marked by a black arrow in (a).

Fig. 5 shows the localization of the states as well as spin polarization of $MoTe_2$ for $E = E_F + 60$ meV. The localization is defined as in the previous section and the spin polarization is given in units of $\hbar/2$. The direction of the spin polarization is a consequence of the x to $-x$ mirror symmetry and time-reversal symmetry. The almost pure spin polarization of the topological Fermi arc in y-direction can be clearly seen.

C. Magnetic impurities

1. Magnetic moments and impurity density of states

The introduction of spontaneous magnetization of the impurities may lead to a lifting of the high density of states close to the Fermi energy. This possibility has been considered for the substitutional TM impurities on the relevant ("top" for $MoTe_2$, "bottom" for WTe_2) surfaces, where the surface electronic structure is in best agreement with experimental obser-

TABLE III. Impurity ground state spin moments in μ_B.

system\impurity	TM_{Te1}	TM_{Te2}
WTe_2	0	0.6
$MoTe_2$	0.6	1.4

vations, as discussed above. We find that a spontaneous magnetization of the Mo_{Te} impurity lowers the total energy in both inequivalent Te1 and Te2 positions, while the W_{Te} impurity only becomes magnetic at the Te2 position. The resulting magnetic moments are shown in Tab. III. The overall higher moment of the 4d-impurities (Mo) compared to the 5d-impurities (W) is expected from general trend in the stoner parameter $I_{3d} > I_{4d} > I_{5d}$, predicting a decreasing tendency to develop spontaneous magnetization for d-electron systems with larger d-shell number.

In Fig. 6 the density of states of the substitutional TM impurities at the Te1 and Te2 positions is shown. Compared are the non-magnetic and magnetic calculations of the defects on the relevant surfaces ('bottom' surface of WTe_2 and 'top' surface of $MoTe_2$). A comparison to the experimental data (shown in Fig. 5 of the main text) reveals that for WTe_2 only the non-magnetic W_{Te1} impurity and for $MoTe_2$ either the non-magnetic Mo_{Te1} or the non-magnetic or magnetic Mo_{Te2} impurity is in reasonable agreement with the experimentally obtained STS-spectra (Fig. 5 of the main text).

From the experiment we do not know if the defects are magnetic or not. However, we can tell that there is no indication of a Kondo effect screening the magnetic moments, because it would cause an STS resonance at E_F (possibly followed by an anti-resonance) [49], which is absent here. From a theory point of view, the calculation of the Kondo temperature for such a complex system is beyond our reach. The calculated weak moment of $0.6\mu_B$ for the Mo_{Te1} and W_{Te2} defects could be possibly killed by structural relaxations (not included here). It could also be caused by an overestimation of the exchange interaction within density-functional theory: it is known that both the local spin-density approximation and the generalised gradient approximation tend to overestimate weak spin moments, e.g. in Ni_3Al [68]. Given the only small energy difference between the magnetic and non-magnetic solutions (50-60 meV, see Table II), as well as the small calculated exchange splitting of the order of 0.2eV (Fig. 6), it is likely that these two defects carry in reality no magnetic moment.

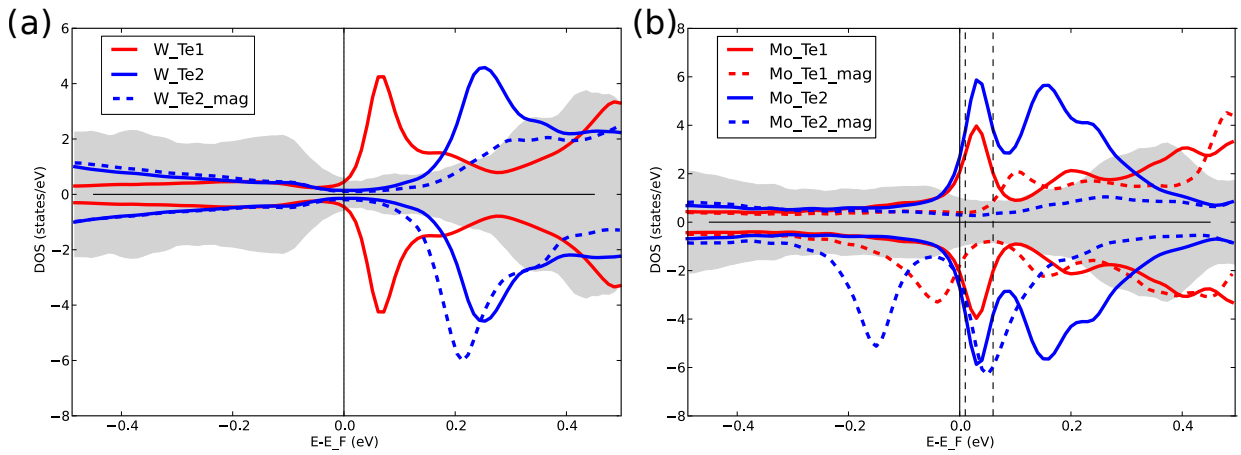

FIG. 6. Density of states of the TM impurities in the Te1 (red) and Te2 (blue) positions in non-magnetic (full lines) and magnetic (dashed lines) configuration. (a) $W_{Te1/2}$ impurity at "bottom" surface of WTe_2. In the Te1-position no magnetic moments is stabilized and the dashed and full red lines fall on top of each other. (b) $M_{Te1/2}$ impurity at "top" surface of $MoTe_2$. The dashed lines in (b) indicate $E - E_F = 10\,\text{meV}$ and $E - E_F = 60\,\text{meV}$.

The situation is different for Mo_{Te2}, where the calculated moment is considerable ($1.4\mu_B$) and is not likely to be removed by relaxations or corrections to the density functional.

2. Backscattering amplitude and protection against inter-arc scattering

To highlight the spin-protection mechanism of the spin-polarized arc-like features in the surface electronic structure of $MoTe_2$ the scattering probability rate $P_{\boldsymbol{k}\boldsymbol{k}_{in}}$, describing the transition rate for an incoming Bloch electrons with wavevector $\boldsymbol{k}_{in}$ being scattered to $\boldsymbol{k}$ is shown for the magnetic $Mo_{Te2,mag}$ impurity at $E_F+10\,\text{meV}$ and $E_F+60\,\text{meV}$ in a logarithmic color scale in Fig. 7. This particular impurity has been chosen for this analysis, since, on the one hand, the strongest magnetic moment was found at this positions (cf. Tab. III) and, on the other hand, the resonance in the majority spin-channel shows up very close to $E_F+60\,\text{meV}$, which should therefore have the largest effect on the scattering rates, observable in the QPI measurements and exJDOS simulations at this energy due to resonant behavior of the impurity.

For both energies shown here the initial wavevector ($\boldsymbol{k}_{in}$) was chosen in the Fermi-arc slightly off from the high symmetry line at $k_y = 0$. As the color scale illustrates, an electron

with wavevector $\boldsymbol{k}_{in}$ is predominantly scattered within the same arc (intra-arc scattering, small scattering angle $\boldsymbol{q} = \boldsymbol{k} - \boldsymbol{k}_{in}$) and even though time-reversal symmetry is broken, the backscattering amplitude (at $\boldsymbol{k} = -\boldsymbol{k}_{in}$) is strongly suppressed and several orders of magnitude smaller than other scattering channels. It can thus be concluded that the spin-protection mechanism outweighs the formally allowed backscattering off a single magnetic impurity. To see a larger effect, one possibility would be that several magnetic impurities cluster ferromagnetically, forming a larger defect with larger effective moment, as recently demonstrated in the Mn-doped topological insulator Bi_2Te_3 [43].

3. The exJDOS for different non-magnetic and magnetic impurities in $MoTe_2$

In Fig. 8 the exJDOS images at $E = E_F - 50\,\text{meV}$ are shown for the non-magnetic Mo_{Te1} and Mo_{Te2} impurities as well as for the magnetic Mo_{Te2} impurity on the "top" surface. Overall, similar features are visible for all impurities. Especially the relative intensity of the surface-resonance-associated signature (highlighted with white dashed ellipses) is not particularly pronounced compared to all the other features stemming from scattering processes involving trivial surface-projected bulk bands. This is in agreement with the experimental observation shown in the top panel of Fig.4(c) in the main text.

For $E = E_F + 10\,\text{meV}$ and $E = E_F + 60\,\text{meV}$ the exJDOS images for the non-magnetic and magnetic $\text{Mo}_{\text{Te1/2}}$ impurities are plotted on the "top" surface of $MoTe_2$ in Fig. 9. The comparison between magnetic and non-magnetic defects shows only a negligible change in the resulting exJDOS images, which is in agreement with the only very small backscattering rate that is introduced by the magnetic impurity (cf. Fig. 7). A larger difference can be seen between Te1 and Te2 positions of the impurity. Thus a significant contribution to the QPI signal due to spontaneously magnetized impurities can be excluded. In agreement with the experimental data discussed in the main text (Fig. 4(c)) an arc-like shape in the QPI images can be seen quite clearly for the Mo_{Te1} impurity (white dashed line) at $E = E_F + 10\,\text{meV}$, which is then strongly suppressed due to the spin-texture of the arc at $E = E_F + 60\,\text{meV}$ (signal inside the white-dashed ellipse).

The comparison of exJDOS images at the different energies with the overall shape of STS-QPI data presented in the main text reveals that the best agreement is found for the Mo_{Te1} impurity, which is consistent with the LDOS of the impurity and the measured STS

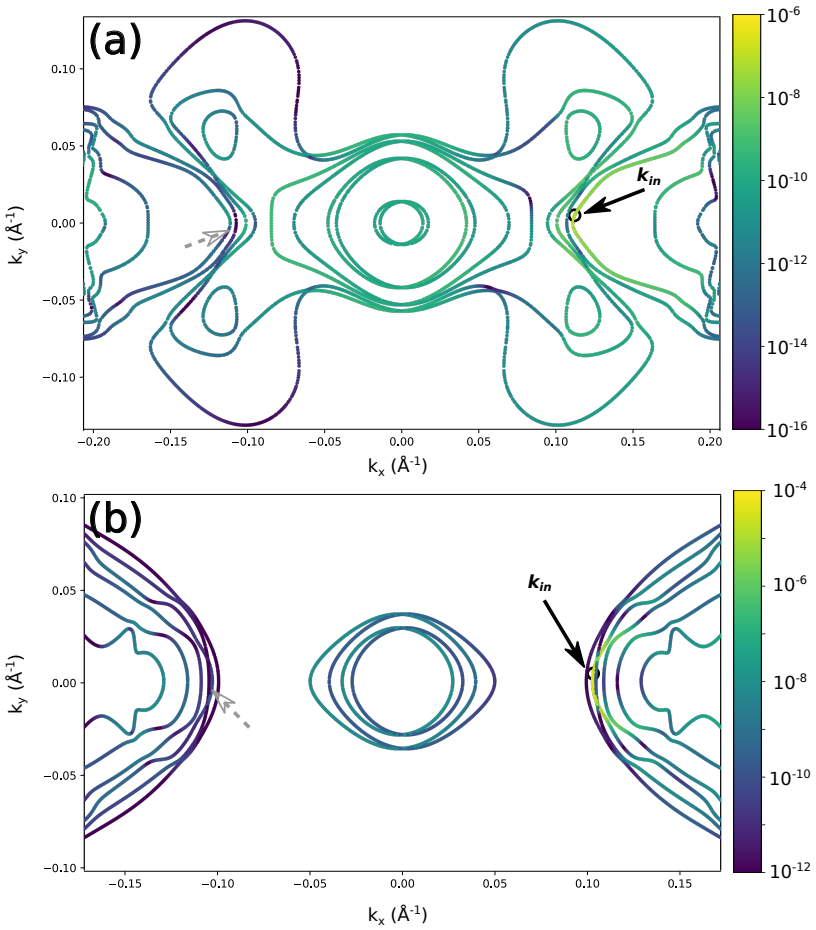

FIG. 7. Scattering probability off a $\mathrm{Mo}_{\mathrm{Te2,mag}}$ impurity for an incoming wave (denoted $\boldsymbol{k}_{in}$) coming from the arc-like surface state for (a) $E_F + 10\,\mathrm{meV}$ and (b) $E_F + 60\,\mathrm{meV}$. The color codes on the constant energy contours (CECs) shown in a logarithmic scale the scattering probability amplitude (in fs/at% per line segment of the CEC) for a transition of the incoming wave $\boldsymbol{k}_{in}$ to all possible final states on the CEC. Although the impurity in this example is magnetic with a resonance in one spin channel close to $E_F + 60\,\mathrm{meV}$ (cf. DOS in Fig. 6), which is considered in (b), forward scattering dominates over time-reverse backscattering ($\boldsymbol{k}_{in} \to -\boldsymbol{k}_{in}$, marked with gray-dashed arrow) by several orders of magnitude.

spectra (Fig. 5 of the main text).

4. Simulation of exJDOS images for different non-magnetic and magnetic defects in WTe_2

The simulation of the exJDOS images for different W_{Te} impurities (Te1, Te2, magnetic and non-magnetic) are summarized in Fig. 10 for the "bottom" surface at $E = E_F$. In

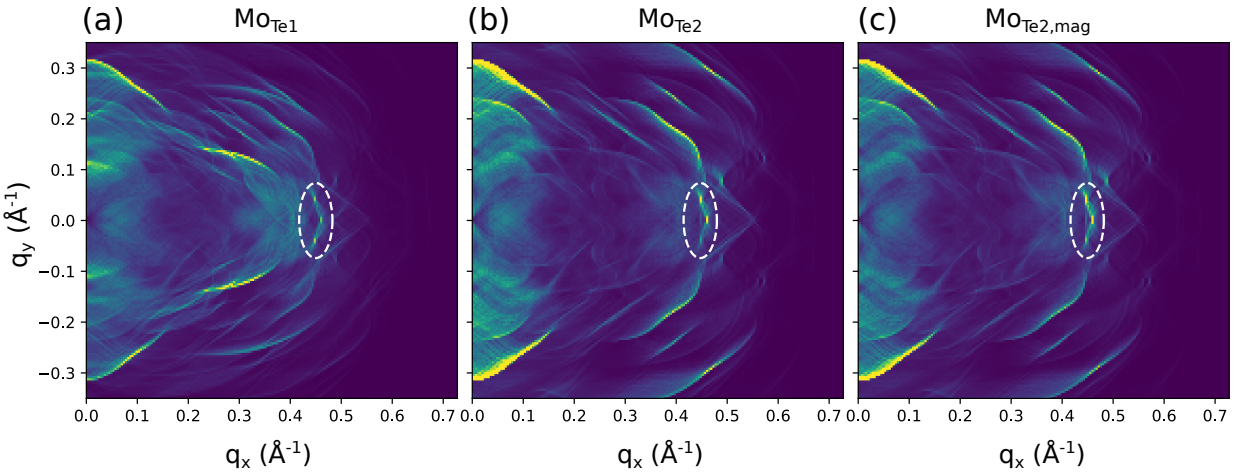

FIG. 8. exJDOS at $E_F - 50\,\text{meV}$ for (a) Mo_{Te1}, (b) Mo_{Te2}, and (c) $\text{Mo}_{\text{Te2,mag}}$ impurities. The feature associated to the surface resonance state occurs in the region highlighted with the white dashed ellipse. In agreement with experimental observations the surface-resonance features is only very weak as compared to other contributions to the QPI.

addition to the high-intensity feature centered around $\boldsymbol{q} = 0$, the most prominent feature is the arc-like shape associated to inter-arc scattering in the trivial surface states of WTe_2. This open-arc-shaped feature shows a depression of the intensity around the tip of the arc at $\boldsymbol{q} \approx (0.42, 0)$ for both magnetic and non-magnetic impurities in accordance to the low backscattering rate and the strong protection against exact backscattering by the surface arcs spin-texture.

D. Used Software packages

The images for the crystal structures in this work were produced with the *VESTA* software [69]. The 3D plots for the bulk band structure were plotted using *Paraview* [70] whereas 2D plots were done with the help of the *Matplotlib* library [71] in *python*.

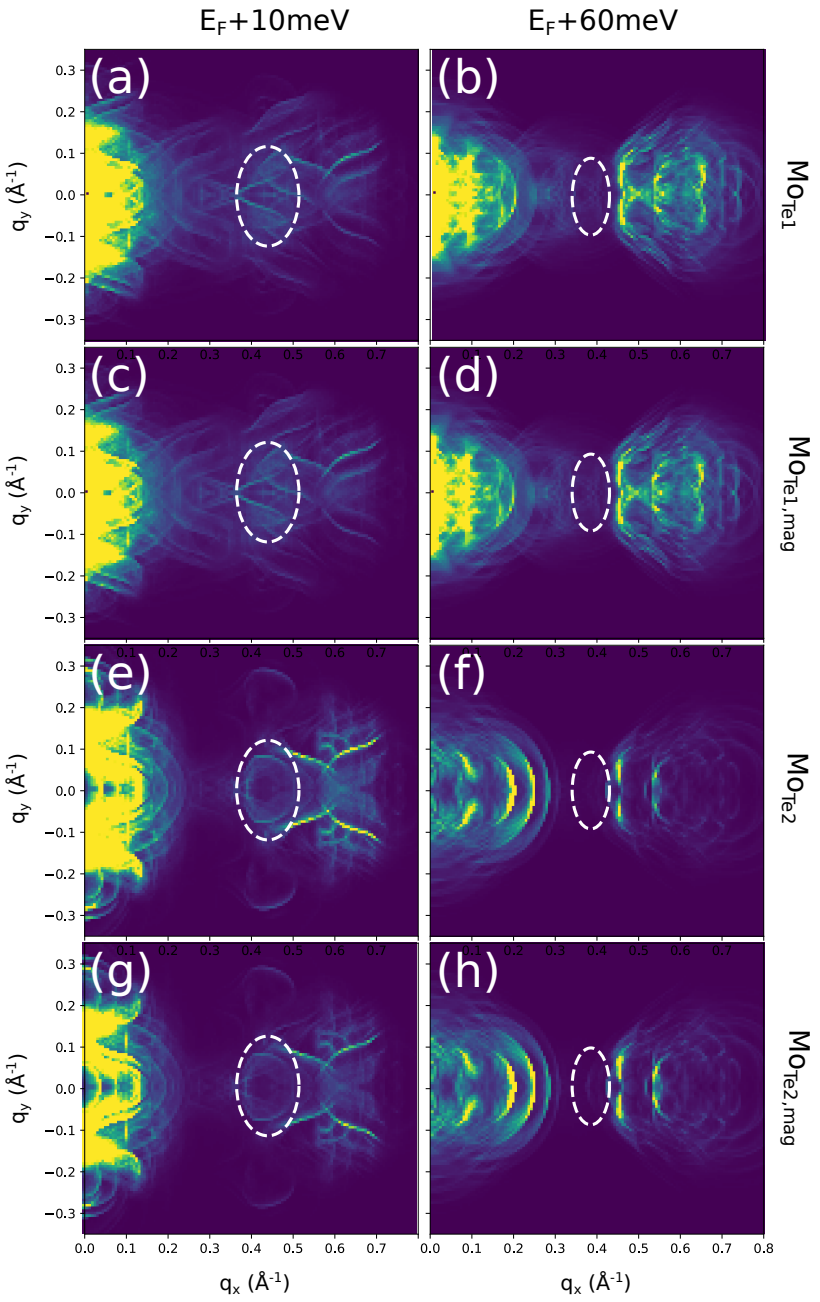

FIG. 9. exJDOS at $E_F + 10\,\text{meV}$ (left column) and at $E_F + 60\,\text{meV}$ (right column) for different Mo_{Te} impurities: (a,b) non-magnetic Mo_{Te1}, (c,d) magnetic Mo_{Te1}, (e,f) non-magnetic Mo_{Te2}, and (g,h) magnetic Mo_{Te2} impurities. The contributions from the arc-like surface state is highlighted with a white dashed line ($E_F + 10\,\text{meV}$, left column) and a white dashed ellipse ($E_F + 60\,\text{meV}$, right column).

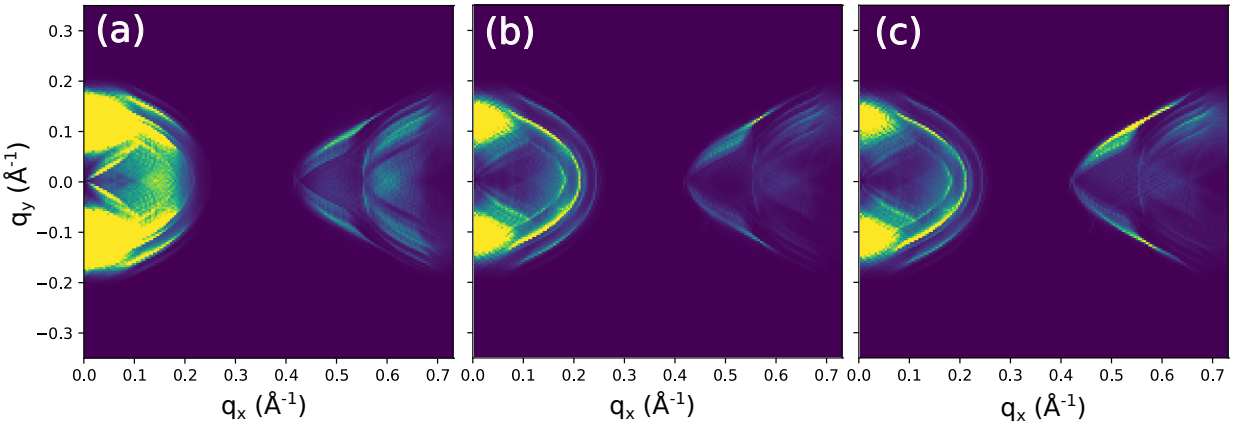

FIG. 10. exJDOS image for different W_{Te} impurities on the "bottom" surface of WTe_2: (a) non-magnetic W_{Te1}, (b) non-magnetic W_{Te2}, and (c) magnetic W_{Te1} defects. All impurities show common features of an arc-like structure in the simulated QPI images with a suppression around the center of the arc at $q_y = 0$ due to the spin-protection mechanism in the scattering process even in the case of a single magnetic defect [shown in (c)].

II. EXPERIMENTAL DETAILS

A. Methods

High quality single-crystals were grown by chemical vapor transport. High-purity W/Mo and Te metals were sealed in a quartz ampule together with iodine used as the transport agent. The stoichiometry of the products was confirmed by X-ray fluorescence spectroscopy. The room-temperature crystal structures were characterized by reflection-geometry X-ray diffraction. The diffraction data and crystal structure refinement results compared well with literature values [72]. The monoclinic structure of MoTe2 at room temperature was additionally confirmed by Raman scattering spectroscopy.

STM measurements have been performed in an ultrahigh vacuum system equipped with a cryogenic STM. After insertion into the system, samples have been cleaved at room temperature at a base pressure of $3 \cdot 10^{-11}$ mbar and immediately inserted into the STM operated at $T = 4.8$ K. All measurements have been performed using electrochemically etched tungsten tips. Spectroscopic data have been obtained using the lock-in technique and a bias voltage modulation in between 1 and 10 meV (r.m.s.) at a frequency of 793 Hz, with the amplitude progressively increasing with the scanning bias. dI/dU maps have been acquired simultaneously to topographic images in constant current mode.

B. Impurity resonances

All measured impurities show the same behavior. This is not surprising since they are all of the same origin: W and Mo substituting Te in WTe_2 and $MoTe_2$, respectively. These are the only two impurities found in our crystals. This is illustrated in Fig. 11. Although some differences in the peak intensity are visible, all impurities are characterized by the emergence of resonances always locked at the very same energy, i.e. slightly above and slightly below +50 meV with respect to the Fermi level for WTe_2 and $MoTe_2$, respectively.

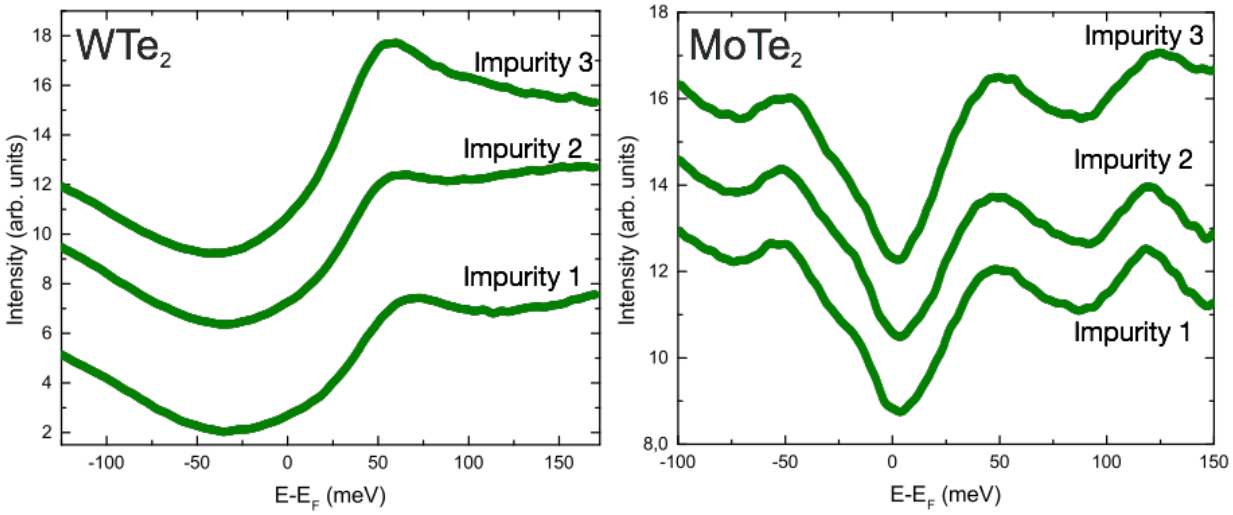

FIG. 11. Scanning tunneling spectroscopy data acquired by positioning the tip over different defects in WTe_2 (left panel) and $MoTe_2$ (right panel). All defects have the very same origin: W and Mo substituting Te in WTe_2 and $MoTe_2$, respectively.